ADVANCED FUNCTIONAL MATERIALS
www.afm-journal.de

www.MaterialsViews.com

Enhanced Performance of Self-Assembled Monolayer Field-Effect Transistors with Top-Contact Geometry through Molecular Tailoring, Heated Assembly, and Thermal Annealing

Nathan Cernetic, Tobias Weidner, Joe E. Baio, Hao Lu, Hong Ma, and Alex K.-Y. Jen**

Low-voltage self-assembled monolayer field-effect transistors (SAMFETs) that operate under an applied bias of less than −3 V and a high hole mobility of 10^{-2} cm^2 V^{-1} s^{-1} are reported. A self-assembled monolayer (SAM) with a quaterthiophene semiconducting core and a phosphonic acid binding group is used to fabricate SAMFETs on both high-voltage (AlO_x/300 nm SiO_2) and low-voltage (HfO_2) dielectric platforms. High performance is achieved through enhanced SAM packing density via a heated assembly process and through improved electrical contact between SAM semiconductor and metal electrodes. Enhanced electrical contact is obtained by utilizing a functional methylthio head group combined with thermal annealing post gold source/drain electrode deposition to facilitate the interaction between SAM and electrode.

1. Introduction

Self-assembled monolayers (SAMs) are now an ubiquitous tool for interface modifications[1] to control and modulate a variety of devices such as hybrid and organic photovoltaics,[2–6] light-emitting diodes,[7–10] and organic transistors.[11–15] Recent progress has also expanded the role of SAMs from a passive interfacial modifier to potentially serve as an active device layer to replace traditional dielectrics and semiconductors in organic field-effect transistors (OFETs). For example, the development of hybrid dielectrics, which are comprised of an ultrathin high-*k* metal oxide layer in conjunction with an SAM, enables low-voltage high-performance operation of organic transistors.[16–18]

Self-assembled monolayer field-effect transistors (SAMFETs) are a promising concept that uses rationally designed π-conjugated SAMs as the semiconductor of a transistor.[19–23] This concept works in principle because charge transport in an organic semiconductor-based FET occurs in the first few monolayers closest to the dielectric.[24,25] SAMFETs are believed to have a broad appeal for organic semiconductor device applications due to their low-cost processing, reduced material quantity needed compared to tradition organic thin film transistors, and ability to be used toward flexible electronics and sensing applications. Significant progress has been made through molecular design and novel device architecture to achieve a state-of-the-art hole mobility of around 10^{-2} cm^2 V^{-1} s^{-1}.

In order to achieve further performance enhancement, it is critical to overcome a fundamental challenge of efficient contact between the metal source/drain electrodes and SAM semiconductor in SAMFET devices. Efficient contacts between SAM semiconductor and electrodes may have been enabled by Smits et al. through under-etching the electrodes allowing the SAM to form underneath or, as shown by Schmaltz et al., through utilizing a secondary SAM to elevate the electrodes to allow edge-on contact with the SAM semiconductor core.[20,21] However, these reports utilize cumbersome and complicated device architectures that may make SAMFETs less appealing toward commercialization. Furthermore, little work has been done to examine the impact of SAM processing on molecular packing density.

Herein we demonstrate top-contact bottom-gate low-voltage p-type SAMFETs with a hybrid hafnium oxide (HfO_2) dielectric that operates under a bias of −3 V and has a charge carrier mobility of 10^{-2} cm^2 V^{-1} s^{-1}. Charge carrier mobility of the SAMFET is increased by over two orders of magnitude through the designed functional SAM terminal group that enables efficient charge injection between metal electrode and SAM

N. Cernetic, Prof. H. Ma, Prof. A. K.-Y. Jen
Department of Materials Science
and Engineering, Box 352120
University of Washington
Seattle, WA 98195-2120, USA
E-mail: hma@u.washington.edu ;
ajen@u.washington.edu
Prof. T. Weidner, Dr. H. Lu
Max Planck Institute for Polymer Research
Ackermannweg 10, 55128 Mainz, Germany
Prof. J. E. Baio
School of Chemical, Biological
and Environmental Engineering
Oregon State University
Corvallis, OR 97331, USA
Prof. A. K.-Y. Jen
Department of Chemistry
Box 351700
University of Washington
Seattle, WA 98195-1700, USA

DOI: 10.1002/adfm.201501263

© 2015 WILEY-VCH Verlag GmbH & Co. KGaA, Weinheim

semiconductor in conjunction with optimized processing conditions to enhance SAM packing density.

2. Results and Discussion

The SAM molecules, (11-(5‴-(4-(methylthio)butyl)-[2,2′:5′,2″:5″,2‴-quaterthiophene]-5-yl)undecyl)phosphonic acid (MTB4TC11) and (12-(5‴-(4-(methylthio)butyl)-[2,2′:5′,2″:5″,2‴-quaterthiophene]-5-yl)dodecyl)phosphonic acid (MTB4TC12), used in this study are designed in such a manner to promote efficient charge injection between the semiconducting core and chosen electrode. As shown in **Figure 1**a, the molecule is comprised of a phosphonic acid binding group which allows for the covalent attachment to a variety of metal oxides.[26] A flexible undecyl or dodecyl spacer unit is chosen to promote self-assembly and optimal π–π overlap due to its conformational freedom.[27] A quaterthiophene unit is chosen as the semiconducting core due to its proven ability to work as a semiconductor in both thin film[27] and monolayer[28] transistors. Finally, to achieve efficient charge injection into the SAM a functional terminal group composed of methylthiobutyl is chosen. In order to enhance charge injection and minimize contact resistance, the terminal group is designed to take advantage of the well-known gold-sulfide coordinate bond that occurs between the two species.[29] In particular, methylsulfide has been used in the past as an anchoring group for molecular junctions due to its ability to electronically couple with gold.[30] To take advantage of this intimate contact, a simple top-contact bottom-gate transistor architecture is used (Figure 1b). This will simplify the device architecture compared to those reported for previous high-performance SAMFETs.[20,21]

In order to better understand the dynamics of the coordinate bond between the SAM molecules and gold electrodes high-voltage SAMFETs are first fabricated and the impact of thermal annealing on device performance is also examined. SAMs are assembled via immersion at room temperature on a traditional dielectric platform (Figure 1b) previously used by our group for both thin film transistors[31] and SAMFETs.[32] After SAM assembly and cleaning to remove aggregates, substrates are annealed either before or after gold electrode deposition at 120 °C for 10 h. Remarkably, **Figure 2** a shows a considerable

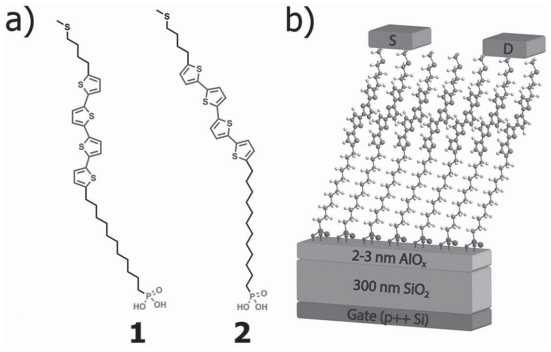

Figure 1. a) Molecular structures of SAM semiconductors used in this study, **1** MTB4TC11 and **2** MTB4TC12; b) schematic of high-voltage SAMFETs fabricated.

shift in performance comparing devices that are not annealed, annealed before electrode deposition, and annealed after electrode deposition. Devices not annealed show no performance with the inability to act as a switch. Figure 2b shows that devices annealed before electrode deposition have some limited charge mobility of around 10^{-5} cm^2 V^{-1} s^{-1} while devices annealed after electrode deposition show two orders of magnitude increase in charge mobility to 10^{-3} cm^2 V^{-1} s^{-1}.

In terms of yield, roughly half of all devices annealed before electrode deposition function properly, while the yield for devices annealed after electrode deposition is near unity. Interestingly, this enhancement is accompanied by a shift in apparent threshold voltage (V_t) as can be seen in Figure 2 c. Devices annealed before or after electrode deposition exhibited an apparent threshold voltage of around –80 V and –65 V, respectively. While V_t remains constant across tested channel lengths regardless of odd or even alkyl chain of SAMFET molecules, the impact of annealing before or after electrode deposition plays a clear role and elucidates a potential mechanism for the shown performance enhancement.

V_t is generally thought to be related to the surface density of deeply trapped charges in the channel and contact region of a transistor.[33] Deep traps, which are considered to be a few kT above the highest occupied molecular orbital, may occur due to structural defects and impurities.[34] It is likely that the deposition of gold on top of the SAM semiconductor resulted in

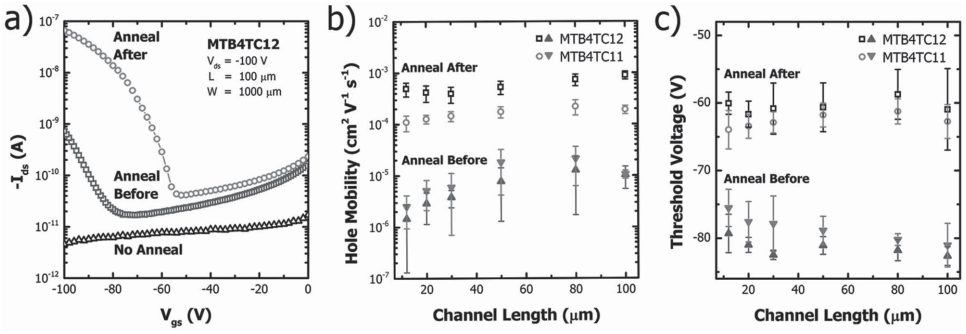

Figure 2. Anneal before indicates SAM annealing at 120 °C for 10 h before electrode deposition and anneal after indicates SAM annealing at 120 °C for 10 h after electrode deposition. a) Characteristic transfer curve for high-voltage SAMFETs with MTB4TC12 semiconductor SAM with different annealing routes. Transistor performance parameters for b) hole mobility and c) threshold voltage based on SAM semiconductor and annealing route. Data are averaged of approximately seven devices per channel length and are for transistors with a channel width of 1000 μm.

© 2015 WILEY-VCH Verlag GmbH & Co. KGaA, Weinheim

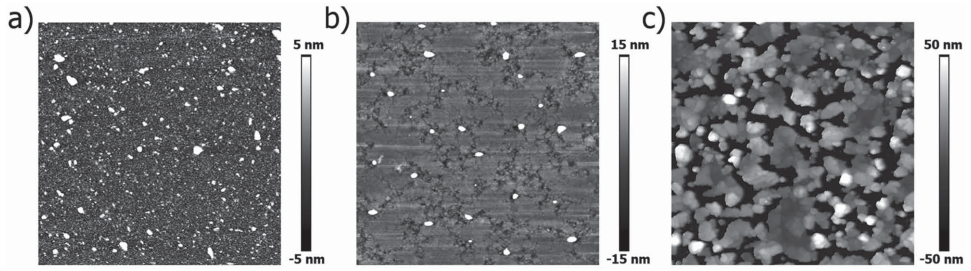

Figure 3. Representative morphology of Au on top of MTB4TC11 SAM assembled on AlO_x measured by tapping mode atomic force microscopy for a) no anneal, b) anneal after, and c) over annealed substrates.

the formation of such trap states through the creation of local structural disorder. Using tapping mode atomic force microscopy (AFM), the morphology of unannealed gold on top of the SAM (**Figure 3**a) shows morphology consistent with having a high density of trap sites due to the numerous small grains and subsequent grain boundaries. However, upon annealing at 120 °C (Figure 3b), these grains coarsen to form large interconnected grains. Evidence of this morphology change indicates that the gold atoms are able to reorganize to a more energetically favorable morphology to allow for better contact between electrode and SAM semiconductor resulting in reduced trap sites. This reduction in trap site density due to grain coarsening may also be a contributing factor for the mobility enhancement that occurs upon annealing post electrode deposition.

Another mechanism for enhanced mobility is most likely related to a reduced charge injection barrier at the Au–SAM interface. A threshold voltage shift accompanied by improved mobility due to changes between metal electrodes and semiconductor has been found earlier for both thin film organic transistors with SAM modified gold electrodes and monolayer MoS_2 transistors with different metal electrodes.[35,36] The reduced charge injection barrier for devices fabricated in this manuscript is thought to be enabled by the intimate contact formed between the sulfur of the SAM semiconductor and the gold atoms. Thermal annealing after gold electrode deposition is needed to further strengthen the coordinate bond between SAM and electrode which requires a separation distance of less than 0.5 nm.[37] It is hypothesized that annealing post electrode deposition provides enough thermal energy for reorganizing SAM molecules, gold atoms, or both to improve contact.

However, it is known that if temperatures are elevated to around 300 °C, the mobile gold atoms will cause the sulfide to desorb from the surface.[38] It was found that over annealing to above 150 °C will result in gold dewetting from the SAM surface and forming isolated islands of gold (Figure 3c). Such a phenomenon is accompanied by a significant reduction in device performance.

In order to further enhance SAMFET performance, SAM immersion assembly temperature is optimized. Traditionally, for the assembly of SAMs, solvents with a dielectric constant (ε_r) between 3 and 5 are found to be optimal. It is believed that if the solvent ε_r is below 3, SAMs tend to form micelles. If greater than 5, solvent will interact too strongly with the SAM and disrupt assembly at the substrate–solution interface.[39,40] In our study, dimethyl sulfoxide (DMSO) was found to provide the greatest solubility allowing for higher SAM solution concentration without forming aggregate. However, DMSO has a relatively high dielectric constant (≈46), which may limit the dense assembly of SAM.

High-voltage SAMFET devices using the same device architecture shown in Figure 1b with varying SAM immersion assembly temperatures were fabricated and characterized. Morphology of SAMs assembled at room temperature and 120 °C was found to be similar for both MTB4TC11 and MTB4TC12. SAMs assembled at room temperature had root mean squared (RMS) roughness values of 0.26 and 0.46 nm for MTB4TC11 and MTB4TC12, respectively, while SAMs assembled at 120 °C had RMS roughness values of 0.33 and 0.43 nm, respectively. Representative morphologies characterized by tapping mode AFM are shown in **Figure 4**a.

The static water contact angle for MTB4TC12 SAMFETs was found to increase slightly from 71.4° ± 0.8° to 76.2° ± 0.9°, respectively, when comparing assembled at room temperature versus 120 °C. This slightly increased contact angle may be indicative of increased SAM density. The relationship between SAM assembly temperature and density is further corroborated from X-ray photoelectron spectroscopy data which suggests an ≈30% increase in SAM density between room temperature and 120 °C assembly conditions (Table S1, Supporting Information). This improved SAM density results in an order of magnitude higher hole mobility as shown in Figure 4b. This follows an expected trend of increasing mobility with respect to assembly temperature from room temperature to 120 °C while other parameters such as on/off current ratio, threshold voltage, and subthreshold swing remain relatively constant regardless of assembly temperature (Figure S2, Supporting Information). Representative transfer and output curves of high-voltage SAMFETs with MTB4TC11 are shown in Figure 4c,d.

To obtain a better insight of the overall quality of SAMs assembled at 120 °C, the SAM/electrode interface, and the impact of annealing, SAMs of MTB4TC11 were characterized with near edge X-ray absorption fine structure (NEXAFS) spectroscopy. NEXAFS can provide chemical identification of specific bonds within SAMs and detailed information about molecular alignment.[41] Substrates with MTB4TC11 SAM were half covered with a 3 nm thick gold layer to allow for the characterization via NEXAFS of MTB4TC11 SAM with or without gold. After gold deposition, a subset of substrates was then annealed at 120 °C for 2 h to determine the influence of both gold and annealing post gold deposition.

Carbon K-edge spectra, collected at an X-ray incident angle of 55°, from annealed/unannealed versions of MTB4TC11

© 2015 WILEY-VCH Verlag GmbH & Co. KGaA, Weinheim

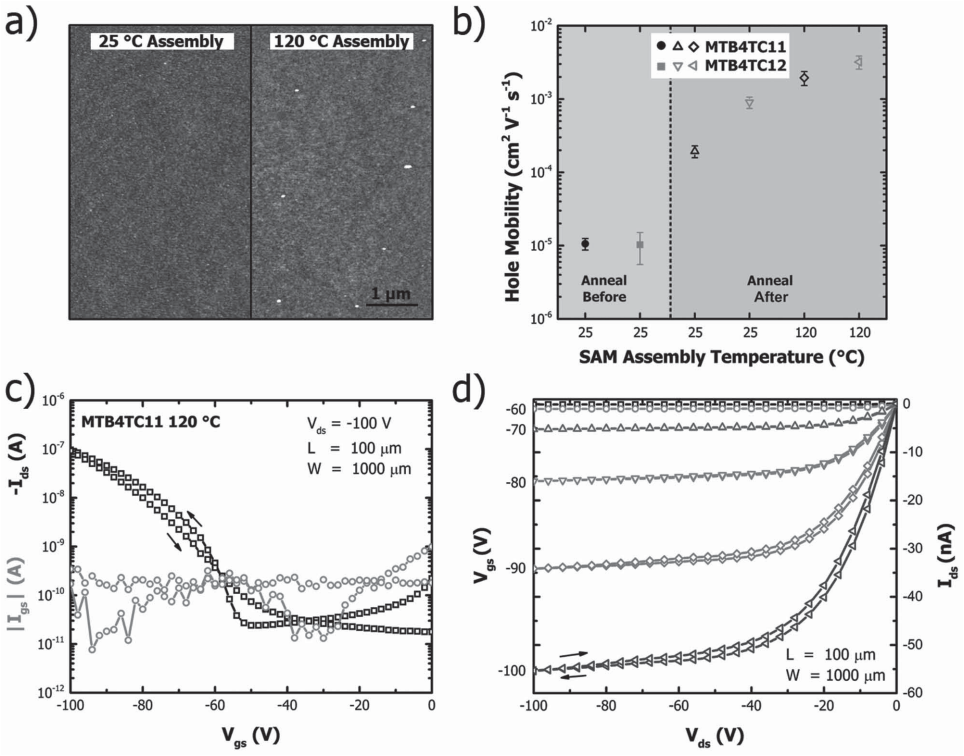

Figure 4. a) Representative morphology measured via AFM of MTB4TC11 SAM on AlO_x assembled at 25 °C (left) and 120 °C (right) with a 5 nm height scale. b) Hole mobility of high-voltage SAMFETs with either MTB4TC11 or MTB4TC12 SAM semiconductor assembled at 25 or 120 °C. The first two left most data points indicate performance for devices annealed before electrode deposition while last four data points indicate performance for devices annealed after electrode deposition. Data are for transistors with channel width and length of 1000 and 100 μm, respectively, and are an average of at least five devices. c) Representative transfer and d) output characteristic transistor curves for an MTB4TC11 SAM assembled at 120 °C SAMFET and annealed after electrode deposition at 120 °C for 10 h with channel width and length of 1000 and 100 μm, respectively.

and Au-coated MTB4TC11 are presented in **Figure 5**a,b. The absorption near 285 eV, related to π^* C=C orbitals within the quaterthiophene groups, is present in all spectra taken from all variants of the MTB4TC11 SAM.[42] Moving to higher X-ray energies we observe a peak at 287 eV related to R*/C—H σ^* molecular orbitals.[43] The orientation and ordering of molecular bonds can be assessed by changes in the X-ray absorption as the sample is rotated relative to the incident X-ray beam by θ. Difference spectra (90°–20°), from annealed/unannealed versions of MTB4TC11 and Au-coated MTB4TC11, are also shown in Figures 5a,b.

In all cases, the NEXAFS spectra show a high degree of ordering (positive dichroism) of π^* C=C molecular orbitals. We have modeled the angle dependence of the π^* resonance to calculate the orientation of the thiophene units before and after gold deposition using standard procedures.[41] Relative to the surface normal, the thiophene tilt angles for unannealed and annealed MTB4TC11 are 29.5° and 30.5°, respectively. This apparent lack in change of tilt angle seems to indicate that annealing by itself may not result in significant molecular reorientation. However, upon depositing gold on top of the MTB4TC11 SAM the thiophene units became more upright. For the unannealed sample set, the thiophene tilt angle is determined to be 26.3°. For the sample set where gold was

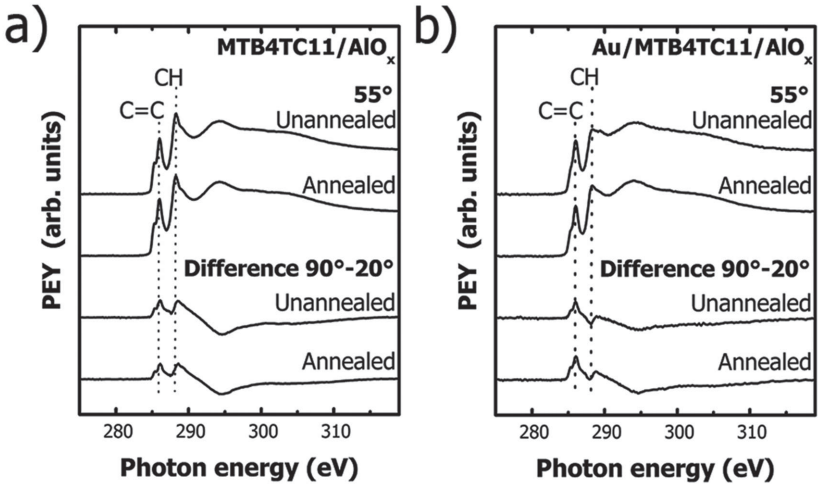

Figure 5. NEXAFS C K-edge spectra from unannealed and annealed samples of a) MTB4TC11 on AlO_x and b) Au-coated MTB4TC11 on AlO_x. Each figure contains spectra collected at X-ray incidence angles of 55° (top traces) along with differences of spectra recorded at 90° and 20° (bottom traces).

© 2015 WILEY-VCH Verlag GmbH & Co. KGaA, Weinheim

annealed after deposition on MTB4TC11 SAM, the thiophene tilt angle is determined to be 24.4°. The SAMs may become more upright when covered with gold due to the proposed coordinate bond between sulfur and gold. Additionally, the greater change in the thiophene tilt angle between pristine SAM and SAM covered with gold (6° and 3° for annealed and unannealed, respectively) indicates annealing with gold facilitates an interaction between SAM and gold. A similar trend with the comparison molecule B4TC11 is also found (Table S2, Supporting Information) which may indicate that the gold is not limited to interact with just the methyl sulfide functional group but may also interact with the sulfur present in the quaterthiophene semiconducting core. The molecular architecture can introduce some uncertainty in the angle determination (twist, torsion angles, etc.). These errors do not apply for systems that use the same molecules: MTB4TC11 or B4TC11 (before and after anneal, or before and after gold deposition). The error margin comparing within a given molecule set is less than 1°. Comparing between datasets we can assume a margin of 2.5°. We have some statistics because we use three different ratios within the dataset to calculate and we get standard deviations of about 0.2°. The rest of the error includes experimental inaccuracies. Errors introduced by data analysis are largely eliminated because we use intensity ratios and not absolute values. So small inaccuracies induced by normalization cancel out. Overall, this NEXAFS dataset provides enough information to show that depositing gold on top of these SAMs results in the thiophenes orienting more upright which is then slightly increased with the addition of an annealing step.

In order to understand the influence of the methylthio functional group a comparison molecule ((11-(5‴-butyl-[2,2′:5′,2″:5″,2‴-quaterthiophene]-5-yl)undecyl)phosphonic acid, B4TC11) was used. Comparing performance data of B4TC11 to MTB4TC11 allows us to further clarify the advantages and disadvantages of the two functional groups. SAMs of B4TC11, MTB4TC11, and MTB4TC12 were assembled on HfO_2 via the heated assembly procedure at 120 °C as described earlier for AlO_x. In order to verify the quality of SAM, static water contact angle for MTB4TC12 was determined at 77.1° ± 0.3° which is comparable to the data previously reported on AlO_x. Additionally, the contact angle of B4TC11 was found to be at 87.3° ± 0.4° which is comparable to literature data.[44] Furthermore, the RMS roughness determined by AFM of MTB4TC12 was found to be 0.32 nm further indicating the presence of a quality monolayer on the HfO_2 dielectric platform (Figure S6, Supporting Information) that is comparable to that of our AlO_x platform.

Performance data for the series of fabricated devices can be seen in **Figure 6**a. Surprisingly, it was found that our control molecule B4TC11 yielded a hole mobility of 0.00213 $cm^2\ V^{-1}\ s^{-1}$ for pristine unannealed devices. However, upon annealing the devices at 120 °C for 10 h after electrode deposition the hole mobility was reduced by nearly an order of magnitude. A similar trend was also seen for an even lower temperature anneal of 80 °C (Figure S7, Supporting Information). This reduction in hole mobility seems to indicate that devices with only a butyl functional head group have limited thermal stability and that annealing results in damage at the SAM/electrode interface. This damage may be caused by diffusion of gold atoms into the SAM semiconductor core resulting in disruption of local SAM molecular order that is integral for charge carrier transport. Comparatively, our MTB4TC11 and MTB4TC12 devices initially exhibit little to no performance without annealing. However, upon annealing after electrode deposition the hole mobility for MTB4TC11 and MTB4TC12 increases to 0.00356 $cm^2\ V^{-1}\ s^{-1}$ and 0.00737 $cm^2\ V^{-1}\ s^{-1}$, respectively. Additionally, since MTB4TC11 has better mobility compared to unannealed B4TC11 and about an order of magnitude higher hole mobility compared to annealed B4TC11 devices, the influence of the methylthio functional group seems to help enhance device mobility as well as increase thermal stability by protecting the semiconducting core from being disrupted by the gold electrodes.

In order to further understand the influence of the SAM functional head group, contact resistance was determined using a modified transmission line method.[45] Contact resistance with respect to gate–source voltage is shown in Figure 6b. It was found that even though MTB4TC12 exhibited the best device performance, the unannealed B4TC11 devices had the lowest contact resistance. This is reasonable given that it has the shortest functional head group of the systems tested. However, as expected, upon annealing after electrode deposition the contact resistance of B4TC11 becomes the highest among tested architectures. This further verifies that the effect of the methylthio functional group seems to help increase thermal stability by protecting the semiconducting core from being disrupted by the gold electrodes upon heating. While high-voltage devices in this paper serve to elucidate the importance of device processing and design for SAMFETs, real-world applications rely on having low-operating voltage devices. Optimized processing conditions have been used to fabricate low-voltage

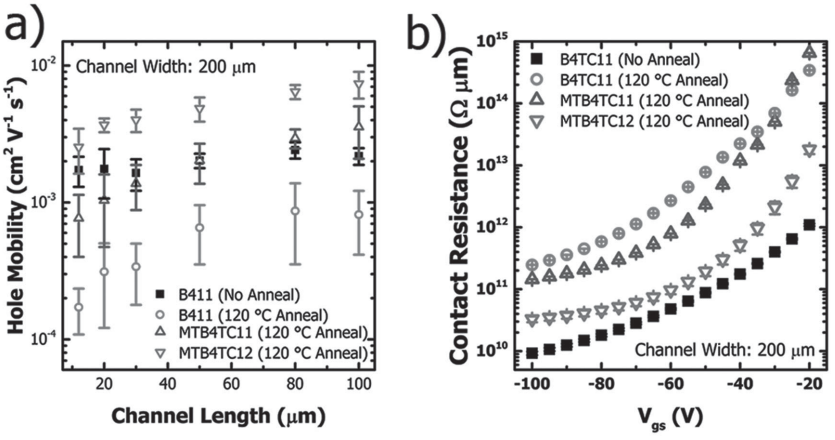

Figure 6. a) Hole mobility with respect to channel length for high-voltage SAMFETs with a HfO_2/300 nm SiO_2/Si dielectric/gate stack and SAM semiconductors B4TC11, MTB4TC11, and MTB4TC12. Performance is indicated if devices are not annealed or are annealed at 120 °C for 10 h after 50 nm Au electrode deposition. b) Contact resistance with respect to gate–source voltage of high-voltage SAMFETs with HfO_2 dielectric stack.

© 2015 WILEY-VCH Verlag GmbH & Co. KGaA, Weinheim

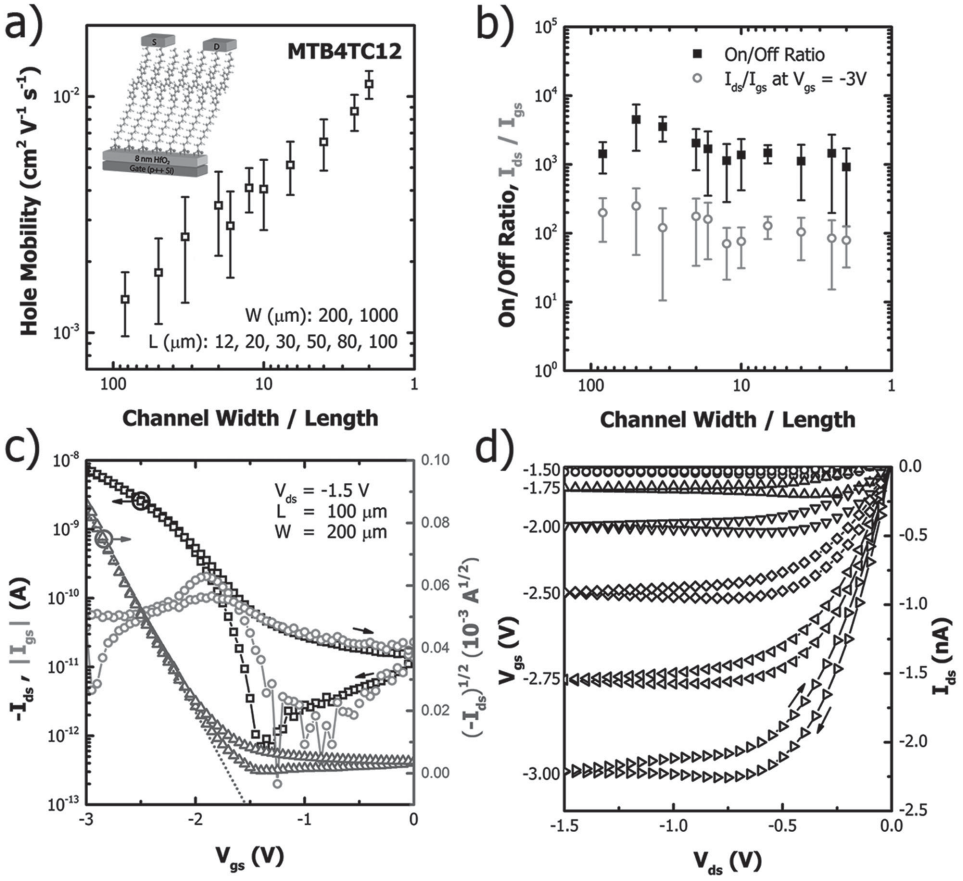

Figure 7. a) Hole mobility with respect to the ratio of channel width/length for low-voltage SAMFET with MTB4TC12 SAM semiconductor with an inset showing device architecture. Device assembled under best conditions with SAM assembly at 120 °C and device annealed at 120 °C for 10 h after gold electrode deposition. b) Transistor performance parameters indicating on/off current ratio, and difference between drain–source current and gate–source leakage current at −3 V. Representative transfer c) and output d) characteristic transistor curves for a device with channel width and length of 200 and 100 μm, respectively, operated at V_{ds} of −1.5 V.

MTB4TC12 SAMFETs on a thin HfO_2 dielectric as seen in the inset of **Figure 7**a. HfO_2 is a proven high-*k* dielectric that has previously been used for low-voltage thin film organic transistors.[46] Fabricated metal–insulator–metal junctions of HfO_2 show a low current density of 2.1×10^{-8} A cm^{-2} at −3 V and capacitance of 565 nF cm^{-2} at a frequency of 1 kHz. However, it is important to take into account the additional capacitance provided by the dodecyl alkyl chain of the MTB4TC12 SAM used which is estimated to lower the total capacitance to 408 nF cm^{-2} (Figure S8, Supporting Information). Low-voltage SAMFETs exhibited excellent charge carrier mobility with the best hole mobility reaching 0.015 cm^2 V^{-1} s^{-1} for devices with channel width and length of 200 and 100 μm, respectively.

Figure 7a shows that mobility increases with decreasing channel width/length ratio indicating that total contact area is critical to device performance. A similar trend is also seen for high-voltage devices and is indicative of performance being limited by resistance within the transistor circuit.[47] As shown in Figure 7b and comparable to high-voltage SAMFETs, on/off current ratios of 10^3 are found which stems from the reduced off current present in low-voltage devices. Additionally, devices are found to have an excellent differential between drain–source current and gate–source leakage current at around 10^2. This exemplifies the high-quality nature of our sol-gel HfO_2 hybrid dielectric as it is currently the highest reported value for low-voltage SAMFET devices. Representative transfer and output characteristics for a device with channel width and length of 200 and 100 μm, respectively, are shown in Figure 7c,d.

3. Conclusion

In summary, high-performance low-operating voltage SAMFETs have been fabricated through the rational design of a functional SAM head group and processing optimization. The methylthiobutyl terminal group of the quaterthiophene-based SAM semiconductors has enabled efficient electrical contact to Au electrodes while maintaining SAMFET thermal stability. Annealing has been shown to further enhance the coordinate bond between SAM and electrode to enable over two orders of magnitude increase in charge carrier mobility. Additionally, through the use of heated immersion assembly, SAM density has been increased by ≈30% resulting in another order of magnitude higher charge carrier mobility. Low-voltage SAMFETs

© 2015 WILEY-VCH Verlag GmbH & Co. KGaA, Weinheim

utilizing hybrid HfO_2 sol-gel dielectric were then assembled under optimized processing conditions to achieve a peak hole mobility of 0.015 $cm^2 V^{-1} s^{-1}$. These results show the importance of terminal group and processing for SAMFETs and should be generally applicable to other SAM semiconductor systems.

4. Experimental Section

SAM Synthesis: Complete synthesis information can be found in the Supporting Information.

Assembly, Device Fabrication, and Characterization of SAMFETs: High-voltage devices were fabricated on cleaned heavily p-doped silicon substrates with a 300 nm thick thermally grown SiO_2. Substrates were then plasma cleaned for 30 min resulting in a 2–3 nm layer of AlO_x as described previously.[18] Low-voltage devices were fabricated on cleaned heavily p-doped silicon substrates with a thin HfO_2 dielectric as described previously.[46] SAMs were assembled by immersing substrates into a filtered 0.1×10^{-3} M SAM solution for 72 h while temperature is held at specific values. Exact details of SAM and HfO_2 processing conditions are available in the Supporting Information. All transistor electrical characterization was completed in an inert environment with an Agilent 4155B semiconductor parameter analyzer.

AFM, Contact Angle Goniometry: Digital Instruments Multimode Nanoscope IIIa scanning probe microscope (Veeco Instruments, Plainview, NY) was used in AFM tapping mode. Aqueous static contact angle values were taken with a VCA Optima Surface Analysis System (Adv. Surface Technology Products, Billerica, MA) and are an average of five measurements with a standard deviation of less than ±3°.

X-Ray Photoelectron Spectroscopy: MTB4TC12 SAM semiconductor was assembled on AlO_x/300 nm SiO_2/Si substrates at 25 and 120 °C, cleaned via sonication in DMSO, tetrahydrofuran (THF), and hexanes then subsequently characterized via X-ray photoelectron spectroscopy. Measurements were performed on a Kratos AXIS Ultra DLD instrument using a monochromatic Al Kα X-ray source and a 0° takeoff angle in hybrid mode. The compositional scans were acquired using an analyzer pass energy of 80 eV. Error bars in the reported data represent the standard deviation of the average of the three spots on two samples. Data analysis was performed with the CASA XPS software package. The results are summarized in Table S1 (Supporting Information).

Near-Edge X-Ray Absorption Fine Structure Spectroscopy: NEXAFS spectra were collected at the National Synchrotron Light Source (NSLS) U7A beamline at Brookhaven National Laboratory, using an elliptically polarized beam with 85% p-polarization. This beamline is equipped with a monochromator (600 lines per millimeter grating) which provides a full width at half maximum resolution of 0.15 eV at the carbon K-edge. At the carbon K-edge, the monochromator energy scale was calibrated using the intense C 1s–π^* transition at 285.35 eV of a graphite transmission grid placed in the path of the X-rays and partial electron yield was monitored by a detector with the bias voltage maintained at −150 V. Samples were mounted to allow rotation and changing the angle between the sample surface and the synchrotron X-rays. The NEXAFS angle is defined as the angle between the incident light and the sample surface. A molecular rotation (twist angle) of 0° was assumed for the tilt angle calculations.[48]

Supporting Information

Supporting Information is available from the Wiley Online Library or from the author.

Acknowledgements

This work was supported by the Air Force Office of Scientific Research (AFOSR FA9550-09-1-0426). A.K.-Y.J. acknowledges the Boeing–Johnson Professorship for its support.

Received: March 29, 2015
Revised: June 3, 2015
Published online: July 28, 2015

[1] H. Ma, O. Acton, D. O. Hutchins, N. Cernetic, A. K. Y. Jen, *Phys. Chem. Chem. Phys.* **2012**, *14*, 14110.
[2] J. Zou, C.-Z. Li, C.-Y. Chang, H.-L. Yip, A. K. Y. Jen, *Adv. Mater.* **2014**, *26*, 3618.
[3] S. K. Hau, H.-L. Yip, O. Acton, N. S. Baek, H. Ma, A. K. Y. Jen, *J. Mater. Chem.* **2008**, *18*, 5113.
[4] A. Abrusci, S. D. Stranks, P. Docampo, H.-L. Yip, A. K. Y. Jen, H. J. Snaith, *Nano Lett.* **2013**, *13*, 3124.
[5] Y. Zang, C.-Z. Li, C.-C. Chueh, S. T. Williams, W. Jiang, Z.-H. Wang, J.-S. Yu, A. K. Y. Jen, *Adv. Mater.* **2014**, *26*, 5708.
[6] N. B eaumont, I. Hancox, P. Sullivan, R. A. Hatton, T. S. Jones, *Energy Environ. Sci.* **2011**, *4*, 1708.
[7] Y. Zhao, L. Duan, D. Zhang, G. Dong, J. Qiao, L. Wang, Y. Qiu, *ACS Appl. Mater. Interfaces* **2014**, *6*, 4570.
[8] J. S. Park, B. R. Lee, J. M. Lee, J.-S. Kim, S. O. Kim, M. H. Song, *Appl. Phys. Lett.* **2010**, *96*, 243306.
[9] S. G. J. Mathijssen, P. A. van Hal, T. J. M. van den Biggelaar, E. C. P. Smits, B. de Boer, M. Kemerink, R. A. J. Janssen, D. M. de Leeuw, *Adv. Mater.* **2008**, *20*, 2703.
[10] J. G. C. Veinot, T. J. Marks, *Acc. Chem. Res.* **2005**, *38*, 632.
[11] S. A. DiBenedetto, A. Facchetti, M. A. Ratner, T. J. Marks, *Adv. Mater.* **2009**, *21*, 1407.
[12] D. O. Hutchins, T. Weidner, J. Baio, B. Polishak, O. Acton, N. Cernetic, H. Ma, A. K. Y. Jen, *J. Mater. Chem. C* **2013**, *1*, 101.
[13] S. Yogev, R. Matsubara, M. Nakamura, U. Zschieschang, H. Klauk, Y. Rosenwaks, *Phys. Rev. Lett.* **2013**, *110*, 036803.
[14] D. Liu, X. Xu, Y. Su, Z. He, J. Xu, Q. Miao, *Angew. Chem. Int. Ed.* **2013**, *52*, 6222.
[15] M. Salinas, C. M. Jäger, A. Y. Amin, P. O. Dral, T. Meyer-Friedrichsen, A. Hirsch, T. Clark, M. Halik, *J. Am. Chem. Soc.* **2012**, *134*, 12648.
[16] N. Cernetic, O. Acton, T. Weidner, D. O. Hutchins, J. E. Baio, H. Ma, A. K. Y. Jen, *Org. Electron.* **2012**, *13*, 3226.
[17] D. Liu, Z. He, Y. Su, Y. Diao, S. C. B. Mannsfeld, Z. Bao, J. Xu, Q. Miao, *Adv. Mater.* **2014**, *26*, 7190.
[18] O. Acton, D. Hutchins, L. Arnadottir, T. Weidner, N. Cernetic, G. G. Ting, T. W. Kim, D. G. Castner, H. Ma, A. K. Jen, *Adv. Mater.* **2011**, *23*, 1899.
[19] M. Halik, A. Hirsch, *Adv. Mater.* **2011**, *23*, 2689.
[20] E. C. P. Smits, S. G. J. Mathijssen, P. A. van Hal, S. Setayesh, T. C. T. Geuns, K. A. H. A. Mutsaers, E. Cantatore, H. J. Wondergem, O. Werzer, R. Resel, M. Kemerink, S. Kirchmeyer, A. M. Muzafarov, S. A. Ponomarenko, B. de Boer, P. W. M. Blom, D. M. de Leeuw, *Nature* **2008**, *455*, 956.
[21] T. Schmaltz, A. Y. Amin, A. Khassanov, T. Meyer-Friedrichsen, H. G. Steinruck, A. Magerl, J. J. Segura, K. Voitchovsky, F. Stellacci, M. Halik, *Adv. Mater.* **2013**, *25*, 4511.
[22] A. Ringk, X. Li, F. Gholamrezaie, E. C. P. Smits, A. Neuhold, A. Moser, C. Van der Marel, G. H. Gelinck, R. Resel, D. M. de Leeuw, P. Strohriegl, *Adv. Funct. Mater.* **2013**, *23*, 2016.
[23] A. V. S. Parry, K. Lu, D. J. Tate, B. Urasinska-Wojcik, D. Caras-Quintero, L. A. Majewski, M. L. Turner, *Adv. Funct. Mater.* **2014**, *24*, 6677.
[24] F. Dinelli, M. Murgia, P. Levy, M. Cavallini, F. Biscarini, D. M. de Leeuw, *Phys. Rev. Lett.* **2004**, *92*, 116802.
[25] A. Shehu, S. D. Quiroga, P. D'Angelo, C. Albonetti, F. Borgatti, M. Murgia, A. Scorzoni, P. Stoliar, F. Biscarini, *Phys. Rev. Lett.* **2010**, *104*, 246602.

© 2015 WILEY-VCH Verlag GmbH & Co. KGaA, Weinheim

[26] J. P. Folkers, C. B. Gorman, P. E. Laibinis, S. Buchholz, G. M. Whitesides, R. G. Nuzzo, *Langmuir* **1995**, *11*, 813.
[27] F. Garnier, R. Hajlaoui, A. El Kassmi, G. Horowitz, L. Laigre, W. Porzio, M. Armanini, F. Provasoli, *Chem. Mater.* **1998**, *10*, 3334.
[28] S. A. Ponomarenko, O. V. Borshchev, T. Meyer-Friedrichsen, A. P. Pleshkova, S. Setayesh, E. C. P. Smits, S. G. J. Mathijssen, D. M. de Leeuw, S. Kirchmeyer, A. M. Muzafarov, *Organometallics* **2010**, *29*, 4213.
[29] J. Noh, H. S. Kato, M. Kawai, M. Hara, *J. Phys. Chem. B* **2002**, *106*, 13268.
[30] Y. S. Park, A. C. Whalley, M. Kamenetska, M. L. Steigerwald, M. S. Hybertsen, C. Nuckolls, L. Venkataraman, *J. Am. Chem. Soc.* **2007**, *129*, 15768.
[31] D. O. Hutchins, O. Acton, T. Weidner, N. Cernetic, J. E. Baio, D. G. Castner, H. Ma, A. K. Y. Jen, *Appl. Surf. Sci.* **2012**, *261*, 908.
[32] D. O. Hutchins, O. Acton, T. Weidner, N. Cernetic, J. E. Baio, G. Ting, D. G. Castner, H. Ma, A. K. Y. Jen, *Org. Electron.* **2012**, *13*, 464.
[33] Q.-J. Sun, Z. Xu, S.-L. Zhao, F.-J. Zhang, L.-Y. Gao, Y.-S. Wang, *Synth. Met.* **2010**, *160*, 2239.
[34] S. D. Wang, T. Minari, T. Miyadera, Y. Aoyagi, K. Tsukagoshi, *Appl. Phys. Lett.* **2008**, *92*, 063305.
[35] M. Kitamura, Y. Kuzumoto, S. Aomori, M. Kamura, J. H. Na, Y. Arakawa, *Appl. Phys. Lett.* **2009**, *94*, 083310.
[36] S. Das, H.-Y. Chen, A. V. Penumatcha, J. Appenzeller, *Nano Lett.* **2012**, *13*, 100.
[37] M. Tachibana, K. Yoshizawa, A. Ogawa, H. Fujimoto, R. Hoffmann, *J. Phys. Chem. B* **2002**, *106*, 12727.
[38] D. O. Bellisario, A. D. Jewell, H. L. Tierney, A. E. Baber, E. C. H. Sykes, *J. Phys. Chem. C* **2010**, *114*, 14583.
[39] H.-Y. Nie, M. J. Walzak, N. S. McIntyre, *J. Phys. Chem. B* **2006**, *110*, 21101.
[40] Y. Ito, A. A. Virkar, S. Mannsfeld, J. H. Oh, M. Toney, J. Locklin, Z. Bao, *J. Am. Chem. Soc.* **2009**, *131*, 9396.
[41] J. Stöhr, *NEXAFS Spectroscopy*, Vol. *25*, Springer-Verlag, Berlin **1992**.
[42] H.-J. Himmel, A. Terfort, C. J. Wöll, *J. Am. Chem. Soc.* **1998**, *120*, 12069.
[43] D. A. Outka, J. Stöhr, J. P. Rabe, J. D. J. Swalen, *J. Chem. Phys.* **1988**, *88*, 4076.
[44] M. Novak, A. Ebel, T. Meyer-Friedrichsen, A. Jedaa, B. F. Vieweg, G. Yang, K. Voitchovsky, F. Stellacci, E. Spieker, A. Hirsch, M. Halik, *Nano Lett.* **2011**, *11*, 156.
[45] Y. Xu, R. Gwoziecki, I. Chartier, R. Coppard, F. Balestra, G. Ghibaudo, *Appl. Phys. Lett.* **2010**, *97*, 063302.
[46] O. Acton, M. Dubey, T. Weidner, K. M. O'Malley, T.-W. Kim, G. G. Ting, D. Hutchins, J. E. Baio, T. C. Lovejoy, A. H. Gage, D. G. Castner, H. Ma, A. K. Y. Jen, *Adv. Funct. Mater.* **2011**, *21*, 1476.
[47] Y. Zhang, H. Dong, Q. Tang, Y. He, W. Hu, *J. Mater. Chem.* **2010**, *20*, 7029.
[48] H.-T. Rong, S. Frey, Y.-J. Yang, M. Zharnikov, M. Buck, M. Wühn, C. Wöll, G. Helmchen, *Langmuir* **2001**, *17*, 1582.

© 2015 WILEY-VCH Verlag GmbH & Co. KGaA, Weinheim